RESEARCH ARTICLE
SPACE PHYSICS: MAGNETOSPHERIC PHYSICS

Earth and Planetary Physics
9: 159–170, 2025
doi: 10.26464/epp2024057

Statistical analysis on the validity of the cold plasma approximation for chorus waves based on Van Allen Probe observations and their effects on radiation belt electrons

AoJun Ren, Jiang Yu*, Jing Wang, ZuZheng Chen, and XiaoMan Liu

Planetary Environmental and Astrobiological Research Laboratory (PEARL), School of Atmospheric Sciences, Sun Yat-sen University, Zhuhai Guangdong 519000, China

Key Points:

- Notable differences in chorus wave intensities exist between observations and calculations from the cold plasma approximation.
- Differences between observed and calculated wave intensities enlarge as the plasma density decreases and the geomagnetic activity is enhanced.
- Substantially different electron scattering rates are caused by the cold plasma approximation compared with those by observed wave dispersions.

Citation: Ren, A. J., Yu, J., Wang, J., Chen, Z. Z., and Liu, X. M. (2025). Statistical analysis on the validity of the cold plasma approximation for chorus waves based on Van Allen Probe observations and their effects on radiation belt electrons. *Earth Planet. Phys.*, *9*(1), 159–170. http://doi.org/10.26464/epp2024057

Abstract: Theoretical analysis has demonstrated that the dispersion relation of chorus waves plays an essential role in the resonant interaction and energy transformation between the waves and magnetospheric electrons. Previous quantitative analyses often simplified the chorus dispersion relation by using the cold plasma assumption. However, the applicability of the cold plasma assumption is doubtful, especially during geomagnetic disturbances. We here present a systematic statistical analysis on the validity of the cold plasma dispersion relation of chorus waves based on observations from the Van Allen Probes over the period from 2012 to 2018. The statistical results show that the observed magnetic field intensities deviate substantially from those calculated from the cold plasma dispersion relation and that they become more pronounced with an increase in geomagnetic activity or a decrease in background plasma density. The region with large deviations is mainly concentrated in the nightside and expands in both the radial and azimuthal directions as the geomagnetic activity increases or the background plasma density decreases. In addition, the bounce-averaged electron scattering rates are computed by using the observed and cold plasma dispersion relation of chorus waves. Compared with usage of the cold plasma dispersion relation, usage of the observed dispersion relation considerably lowers the minimum resonant energy of electrons and lowers the scattering rates of electrons above tens of kiloelectronvolts but enhances those below. Furthermore, these differences are more pronounced with the enhancement of geomagnetic activity or the decrease in background plasma density.

Keywords: chorus waves; cold plasma approximation; dispersion relations; scattering rates

1. Introduction

Whistler mode chorus waves are intense right-hand polarized electromagnetic emissions commonly present in the low-density plasmatrough outside the plasmapause (Tsurutani and Smith, 1974, 1977; Meredith et al., 2003; Cao JB et al., 2005, 2007; Gao XL et al., 2014; Zhima et al., 2014; Yu J et al., 2017, 2020a; Liu X et al., 2021). Usually, these waves occur in the frequency range of 0.1–0.8 f_{ce} (where f_{ce} is the equatorial electron cyclotron frequency) and appear in two distinct frequency bands: one is the lower band below 0.5 f_{ce}, and the other is the upper band above 0.5 f_{ce} (e.g., Tsurutani and Smith 1974; Li W et al., 2009; Meredith et al., 2012; Fu XR et al., 2015; Gao XL et al., 2016; Yu J et al., 2018; Chen HY et al., 2021). In addition to the power gap, chorus waves also show a repetitive nature, which is considered to be affected by the electron drift velocity (Lu QM et al., 2021; Gao XL et al., 2022). Generally, chorus waves originate near the geomagnetic equator (Santolík et al., 2003a; Lu QM et al., 2019) and are believed to be generated by cyclotron resonant interaction with energetic electrons with temperature anisotropy ($T_\perp > T_\|$) in the energy range from a few kiloelectron volts to tens of kiloelectron volts (Anderson and Maeda, 1977; Meredith et al., 2001; Li W et al., 2008, 2009; Omura et al., 2009; Fu HS et al., 2012; Liu X and Chen LJ, 2019; Chen ZZ et al., 2022; Wang J et al., 2023a, b).

Through cyclotron resonance with electrons, chorus waves can accelerate seed electrons to ultrarelativistic energies and precipi-

First author: A. J. Ren, renaoj@mail2.sysu.edu.cn
Correspondence to: J. Yu, yujiang5@mail.sysu.edu.cn
Received 27 APR 2024; Accepted 18 JUL 2024.
First Published online 11 OCT 2024.

tate plasma sheet electrons in the Earth's inner magnetosphere, producing the dense outer radiation belt and the pulsating and diffuse aurora (Horne et al., 2005; Bortnik and Thorne, 2007; Ni BB et al., 2008, 2011; Su ZP et al., 2010; Thorne, 2010; Shprits et al., 2012; Thorne et al., 2013; Gao XL et al., 2015, 2024; Li LY et al., 2017; Yu J et al., 2019a, 2022). Usually, the chorus-induced electron diffusions can be quantitatively examined by the quasi-linear scattering rates. To calculate the quasi-linear scattering rates, the resonant wave numbers and frequencies should first be obtained as inputs by simultaneously solving the dispersion relation of the chorus waves and the wave–particle resonant condition (Kennel and Engelmann, 1966; Roth et al., 1999; Summers and Ma CY, 2000; Albert, 2005; Glauert and Horne, 2005). In general, the cold plasma dispersion relation is widely adopted because of its easy applicability in resolving the resonant wave numbers and frequencies (e.g. Albert, 2005; Glauert and Horne, 2005; Summers, 2005; Ni BB et al., 2008, 2011; Su ZP et al., 2009; Li LY et al., 2013, 2017, 2022; Xiao FL et al., 2014; He ZG et al., 2016; Yu J et al., 2020a, 2022). However, the cold plasma approximation is not always applicable, especially when the hot plasmas are abundant, which can strongly affect the evaluation of the wave–particle interaction processes (Ni BB et al., 2017; Chen LJ et al., 2019; Yu J et al., 2019b, 2020b, 2024; Cao X et al., 2020; Ma X et al., 2021). Actually, observations have confirmed that the realistic dispersion relation of chorus waves can deviate substantially from the cold plasma approximation. Hartley et al. (2015, 2016) found, based on the Van Allen Probe observations, that for chorus waves, the converted magnetic field spectral intensities computed by the measured electric spectral intensities and the cold plasma theory deviated more or less from the measured magnetic field spectral intensities. In theory, Chen LJ et al. (2013) predicted that the theoretical dispersion relation of parallel propagation chorus waves can deviate considerably from the cold plasma approximation when abundant hot plasmas are present, which subsequently affects the minimum resonant energy of electrons and their local scattering rates.

In the present paper, we perform a systematic statistical analysis on the validity of the cold plasma dispersion relation of chorus waves for different levels of plasma density and geomagnetic activity based on measurements from the Van Allen Probes from 2012 to 2018. By comparing the chorus-induced electron scattering rates calculated by utilizing the theoretical and statistical dispersion relation, we quantitatively examine the applicability of the cold plasma dispersion relation in evaluating the chorus–electron interaction under different plasma environments and geomagnetic conditions.

2. Data and Methodology

2.1 Wave Measurements and Chorus Identification

The Van Allen Probes, twin satellites launched on August 23, 2012, carried identical instruments to monitor various plasma waves and particle dynamics in the radiation belts. The electromagnetic disturbances and plasma waves were measured by the Electric and Magnetic Field Instrument Suite and Integrated Science (EMFISIS; Kletzing et al., 2013). The Waveform Receiver of EMFISIS provided the averaged spectral matrices of both electric and magnetic fields over the frequency range of 10 to 12 kHz, which can be used to analyze the wave propagation and polarization (wave normal angle, ellipticity, and planarity) by the singular value decomposition method (Santolík et al., 2003b). The High Frequency Receiver of EMFISIS provided a single electric field spectrum in the frequency range of 10 to 400 kHz, which can be used to extract the upper hybrid resonance frequency and thus to infer the plasma density (Kurth et al., 2015).

Chorus waves are identified according to the following criteria: (1) outside the plasmapause with a density value lower than $124 \times (3/L)^4$ cm^{-3} (Sheeley et al., 2001); (2) wave frequencies within the range of 0.1–0.8 f_{ce}; (3) ellipticity >0.7 and planarity >0.6.

Figure 1 presents an event overview of chorus waves observed by Van Allen Probe A during the period of 01:00–10:00 universal time (UT) on October 12, 2012. From top to bottom, Figure 1 shows the plasma density, the electric and magnetic field spectral densities, planarity, ellipticity, and wave normal angles. Van Allen Probe A crosses the plasmapause at 03:00 UT and 08:40 UT when the plasma density changes sharply. Outside the plasmapause (between 03:00 UT and 08:40 UT), intense electromagnetic emissions with large planarity and ellipticity are observed within the frequency range of 0.1–0.8 f_{ce}. Thus, they are identified as chorus waves according to the aforementioned criteria.

2.2 Calculations of Chorus Intensities Under the Cold Plasma Hypothesis

To validate the applicability of the cold plasma approximation for chorus waves, we make a comparison between their observed magnetic field spectral densities and those calculated from their observed electric field spectral densities and the cold plasma dispersion relation. According to previous studies (e.g., Hartley et al., 2016), the magnetic field spectral densities (I_{B_cal}) converted by the electric field spectral densities (I_{E_obs}, as measured by the Van Allen Probes) under the cold plasma hypothesis for chorus waves with arbitrary wave normal angles (θ) can be expressed as follows:

$$I_{B\_cal} = I_{E\_obs}\left(\frac{n}{c}\right)^2 \sin^2\beta, \tag{1}$$

with

$$\beta = \arccos\left[\frac{\sin\theta\left(n^2 - P\right)}{\sqrt{\left(n^2\sin^2\theta - P\right)^2 + \frac{D^2\left(n^2\sin^2\theta - P\right)^2}{\left(n^2 - S\right)^2} + n^4\sin^2\theta\cos^2\theta}}\right], \tag{2}$$

and

$$n^2 = \frac{RL\sin^2\theta + PS\left(1 + \cos^2\theta\right) - \sqrt{\left(RL\sin^2\theta + PS\left(1 + \cos^2\theta\right)\right)^2 - 4PRL\left(S\sin^2\theta + P\cos^2\theta\right)}}{2\left(S\sin^2\theta + P\cos^2\theta\right)}, \tag{3}$$

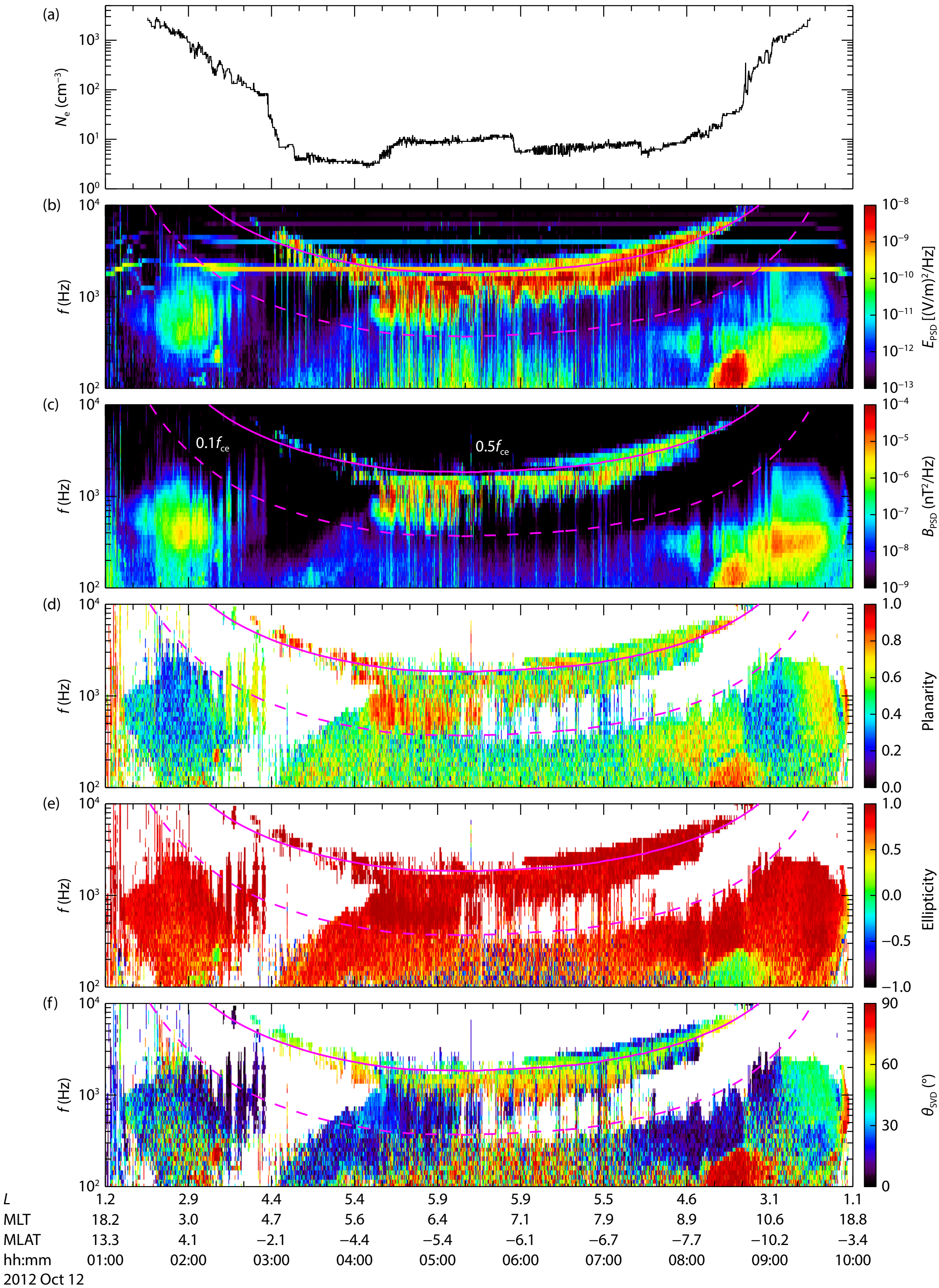

Figure 1. Overview of a chorus wave event observed by Van Allen Probe A on October 12, 2012. (a) The ambient plasma density. (b–c) The power spectral density of the electric field and magnetic field. (d–f) The planarity, ellipticity, and wave normal angle. The dashed and solid purple lines in (b) to (f) represent 0.1 f_{ce} and 0.5 f_{ce}, respectively.

$$R = 1 - \frac{\omega_{pe}^2}{\omega(\omega + \Omega_{ce})} - \frac{\omega_{pi}^2}{\omega(\omega + \omega_{ci})}, \quad (4)$$

$$L = 1 - \frac{\omega_{pe}^2}{\omega(\omega - \Omega_{ce})} - \frac{\omega_{pi}^2}{\omega(\omega - \omega_{ci})}, \quad (5)$$

$$P = 1 - \frac{\omega_{pe}^2}{\omega^2} - \frac{\omega_{pi}^2}{\omega^2}, \quad (6)$$

$$S = \frac{R + L}{2}, \quad (7)$$

$$D = \frac{R - L}{2}, \quad (8)$$

where ω is the wave frequency, and c is the speed of light; Ω_{ce} and ω_{pe} are the cyclotron frequency and plasma frequency of electrons, respectively; and Ω_{ci} and ω_{pi} are the cyclotron frequency and plasma frequency of protons.

Once the chorus waves are identified, the observed electric field spectral density (I_{E_obs}) is used to obtain the calculated magnetic field spectral density (I_{B_cal}) from the cold plasma approximation based on Equation (1). The calculated (B_{w_cal}) and observed (B_{w_obs}) magnetic field intensities, for later comparison analyses, are then calculated by integrating the calculated (I_{B_cal}) and observed (I_{B_obs}) magnetic field spectral densities over the frequency in the range of 0.1–0.5 f_{ce}, respectively.

2.3 Calculations of Chorus-Induced Electron Scattering Rates

To quantify the effect of different dispersion relations on chorus–electron interaction, we compare the quasi-linear bounce-averaged pitch angle scattering rates calculated by using the statistical and the theoretical dispersion relation. For broadband parallel propagating chorus waves, the quasi-linear bounce-averaged pitch angle scattering rate in a dipole field can be written as follows (e.g., Summers, 2005):

$$\langle D_{\alpha\alpha} \rangle = \frac{1}{T(\alpha_{eq})} \int_0^{\lambda_m} D_{\alpha\alpha} \frac{\cos\alpha}{\cos^2\alpha_{eq}} \cos^7\lambda \, d\lambda, \quad (9)$$

$$D_{\alpha\alpha} = \frac{D_{\mu\mu}}{\sin^2\alpha}, \quad (10)$$

$$D_{\mu\mu} = \frac{\pi}{2} \frac{\Omega_{ce}^2}{B_0^2} \frac{(1-\mu^2)}{\gamma^2} \sum_{j=1}^{N} \left(1 - \frac{\omega_j \mu}{k_j v}\right)^2 \frac{W(\omega_j)\, d\omega_j/dk_j}{|v\mu - d\omega_j/dk_j|}, \quad (11)$$

where $T(\alpha_{eq}) = 1.30 - 0.56\sin\alpha_{eq}$, α and α_{eq} are the local and equatorial pitch angle, respectively; λ and λ_m are the magnetic latitude and electron mirror latitude, respectively; and B_0 is the background magnetic field strength. In addition, $\gamma = (1 - v^2/c^2)^{-1/2}$ is the Lorentz factor, v is the electron velocity, $\mu = \cos\alpha$, $W(\omega_j)$is the wave power spectral density evaluated at the resonance frequency ω_j, k_j is the resonance wave number, and N is the resonant order. The summation in Equation (11) is carried out over all the resonance roots, satisfying the gyroresonance condition (Equation (12)) and the dispersion relation (Equation (13) or (14)). The gyroresonance condition between electrons and parallel propagating chorus waves can be expressed as follows:

$$\omega - kv\mu = \frac{|\Omega_{ce}|}{\gamma}. \quad (12)$$

In this study, we use two dispersion relations of parallel propagating chorus waves to calculate the pitch angle scattering rates. One is the theoretical dispersion relation in a cold plasma:

$$c^2 k^2 = \omega^2 - \frac{\omega \omega_{pe}^2}{\omega - |\Omega_{ce}|}. \quad (13)$$

The other is the statistical dispersion relation based on measurements from the Van Allen Probes. The observational dispersion relation is as follows:

$$k = \omega \sqrt{\frac{I_{B\_obs}}{I_{E\_obs}}}. \quad (14)$$

We first obtain scatter data points of the wave number versus wave frequency and subsequently fit their average values to obtain the statistical dispersion relation of chorus waves.

3. The Validity of the Cold Plasma Approximation

Following previous studies (Hartley et al., 2015; Ma X et al., 2021), we use a direct comparison between the observed magnetic field intensities and those calculated from the theory to test the validity of the cold plasma dispersion relation for chorus waves.

3.1 Plasma Density Effect on the Validity of the Cold Plasma Approximation

To investigate the relationship between the validity of the cold plasma dispersion relation and the plasma density for chorus waves, we organize the data into three different plasma density ranges, that is, N_e < 4 cm^{-3}, 4 < N_e < 8 cm^{-3}, and N_e > 8 cm^{-3}. Figure 2 illustrates the statistical results of the comparisons between the observed magnetic field intensities and those converted from cold plasma theory for lower-band chorus waves in three different plasma density ranges. In Figures 2a–2c, the color represents the number of data points in each bin and the diagonal line separates the regions where the observed magnetic field intensities are larger (below the line) and smaller (above the line) than those converted. Therefore, the cold plasma dispersion relation is most reliable only when the data points fall on the diagonal line, and it becomes less applicable when the data points deviate more from the diagonal line. The data points deviate more or less from the diagonal line, but most of them are distributed in the region within an order of magnitude below the diagonal line, indicating that the observed magnetic field intensities are substantially larger than those converted for most cases; thus, the cold plasma approximation is not that applicable in most cases for chorus waves. In addition, as the plasma density increases, the data points are distributed closer to the diagonal line, implying a greater validity of the cold plasma approximation.

To more intuitively reflect the variation in the validity of the cold plasma approximation with the plasma density, we show the probability distributions of $|\log_{10}(B_{w\_cal}/B_{w\_obs})|$ (where B_{w_cal} and B_{w_obs} are, respectively, the calculated and observed magnetic field intensities) in Figures 2d–2f. The larger values represent larger deviations between the calculations and observations. As the plasma density increases, the probability distributions become more centralized to the left, indicating greater validity of the cold plasma dispersion relation. To make this trend clearer, we

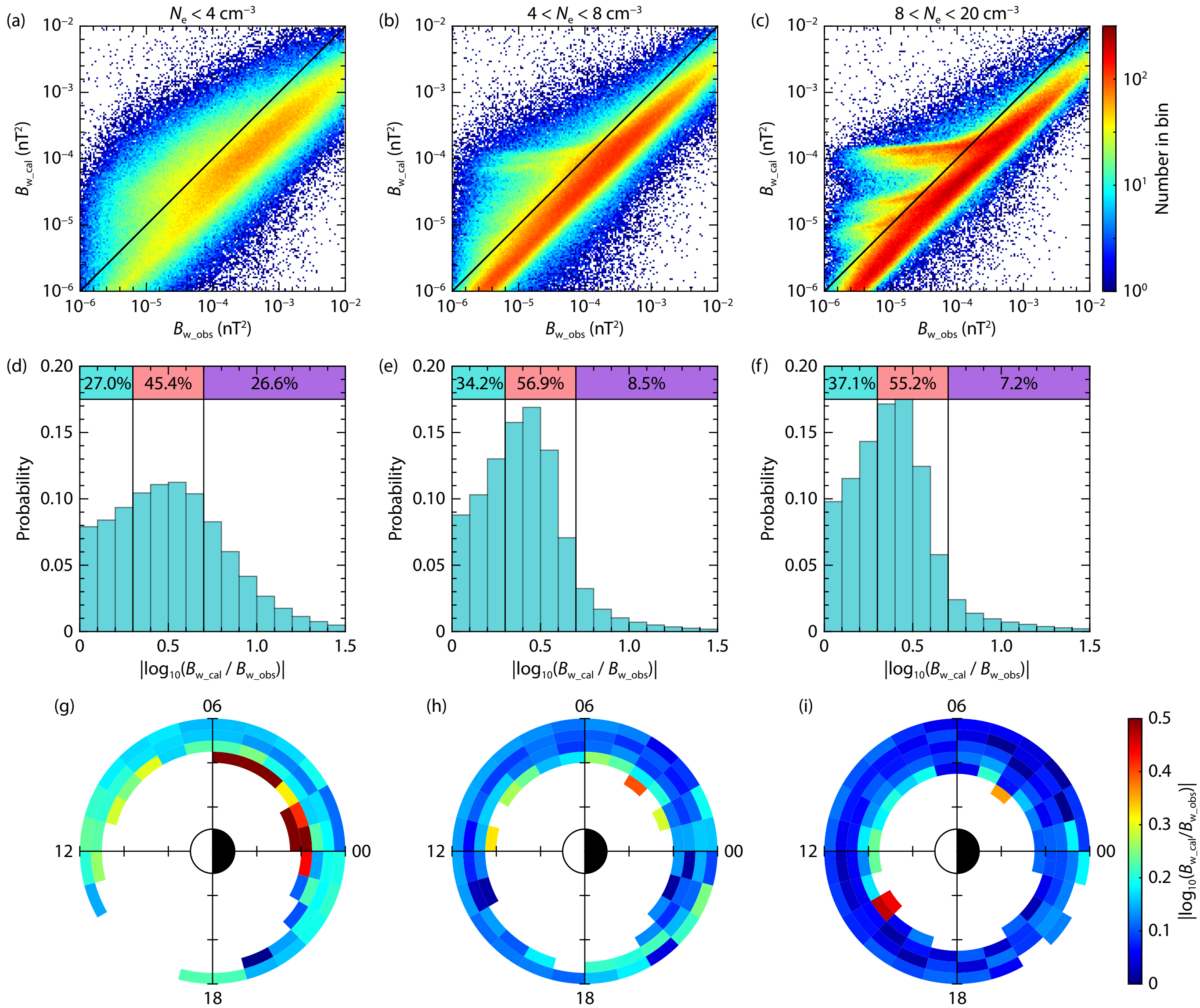

Figure 2. (a–c) Comparisons between the observed magnetic field intensities and those converted from cold plasma theory for lower-band chorus waves in three different plasma density ranges. The color represents the number of data points in each bin, and the diagonal line separates the regions where the observed magnetic field intensities are larger (below the line) and smaller (above the line) than those converted. (d–f) The probability distributions of $|\log_{10}(B_{w\_cal}/B_{w\_obs})|$ in three different plasma density ranges. The percentages of data that occur in three different ratio groups are shown at the top of each panel. The groups from left to right are parameterized as $|\log_{10}(B_{w\_cal}/B_{w\_obs})| < 0.3$, $0.3 < |\log_{10}(B_{w\_cal}/B_{w\_obs})| < 0.7$, and $|\log_{10}(B_{w\_cal}/B_{w\_obs})| > 0.7$. (g–i) Global distribution of averaged $|\log_{10}(B_{w\_cal}/B_{w\_obs})|$ in the L-MLT domain in three different plasma density ranges.

organize the data into two groups (the valid and invalid groups of the cold plasma approximation) and calculate the percentage of data occurring in each group. The valid group is for data with $|\log_{10}(B_{w\_cal}/B_{w\_obs})| < 0.3$ (blue), meaning that the deviations between the calculations and observations are within 2 times. The invalid group is for data with the ratio $|\log_{10}(B_{w\_cal}/B_{w\_obs})| > 0.7$ (purple), meaning that the deviations between calculations and observations are larger than 5 times. The statistical results show that the percentage of data in the valid group increases gradually from 27% in the plasma density range N_e < 4 cm^{-3} to 34.2% and 37.1% in the plasma density range 4 < N_e < 8 cm^{-3} and N_e > 8 cm^{-3}. Conversely, the percentage of data in the invalid group decreases rapidly from 26.6% to 8.5% and 7.2% as the plasma density increases. These changes indicate that the validity of the cold plasma dispersion relation gradually increases with the plasma density. This signature can also be further confirmed by the variation in the averaged $|\log_{10}(B_{w\_cal}/B_{w\_obs})|$ with the plasma density, whose value decreases rapidly as the plasma density increases, as shown in Figure 4a.

To explore where the cold plasma approximation is applicable, we show the global distribution of averaged $|\log_{10}(B_{w\_cal}/B_{w\_obs})|$ in the L-MLT domain in Figures 2g–2i. Large deviations between calculations and observations are mainly distributed in the low-density region from the nightside to dayside through dawnside, especially for those regions on the low L-shell in the dawnside, suggesting that the cold plasma dispersion relation is unreliable in these regions. As the plasma density increases, the deviations rapidly become smaller and the regions of large deviations narrow substantially. In addition, these features again confirm that the validity of the cold plasma dispersion relation gradually increases with the plasma density.

3.2 Substorm Effect on the Validity of the Cold Plasma Approximation

To investigate the relationship between the validity of the cold plasma dispersion relation and the substorms, we organize the data into three geomagnetic activity levels, that is, quiet (AE < 100 nT), moderate (100 nT < AE < 500 nT), and active (AE > 500 nT) conditions (where AE is the auroral electrojet index). Figure 3 illustrates the statistical results in the same figure format as Figure 2. Similarly, the comparison between the observed magnetic field intensities and the calculated values in Figures 3a–3c show that many more data points are distributed below the diagonal line than those above, indicating that the observed magnetic field intensities are substantially larger than those converted for most cases. Therefore, the cold plasma approximation is not that applicable in most cases for chorus waves. As the geomagnetic activity increases, the data points are distributed farther away from the diagonal line, indicating that the validity of the cold plasma dispersion relation gradually decreases with the intensification of substorms, as shown in Figures 3d–3f. The percentage of data in the valid group decreases gradually from 34.2% during the period of quiet conditions to 32.7% and 31.7% during periods of moderate and active conditions, whereas the percentage of data in the invalid group increases rapidly from 9.8% to 13.0% and 16.1% as the geomagnetic activity increases. This signature can be further confirmed by the variation in the averaged $|\log_{10}(B_{w\_cal}/B_{w\_obs})|$ with the substorm, whose value increases rapidly as the geomagnetic activity increases, as shown in Figure 4b. As shown in Figures 3g–3i, the regions where the cold plasma approximation is unreliable are mainly distributed from the duskside to the dawnside through the nightside during the active conditions, especially for those regions on the high L-shell in the nightside. As the geomag-

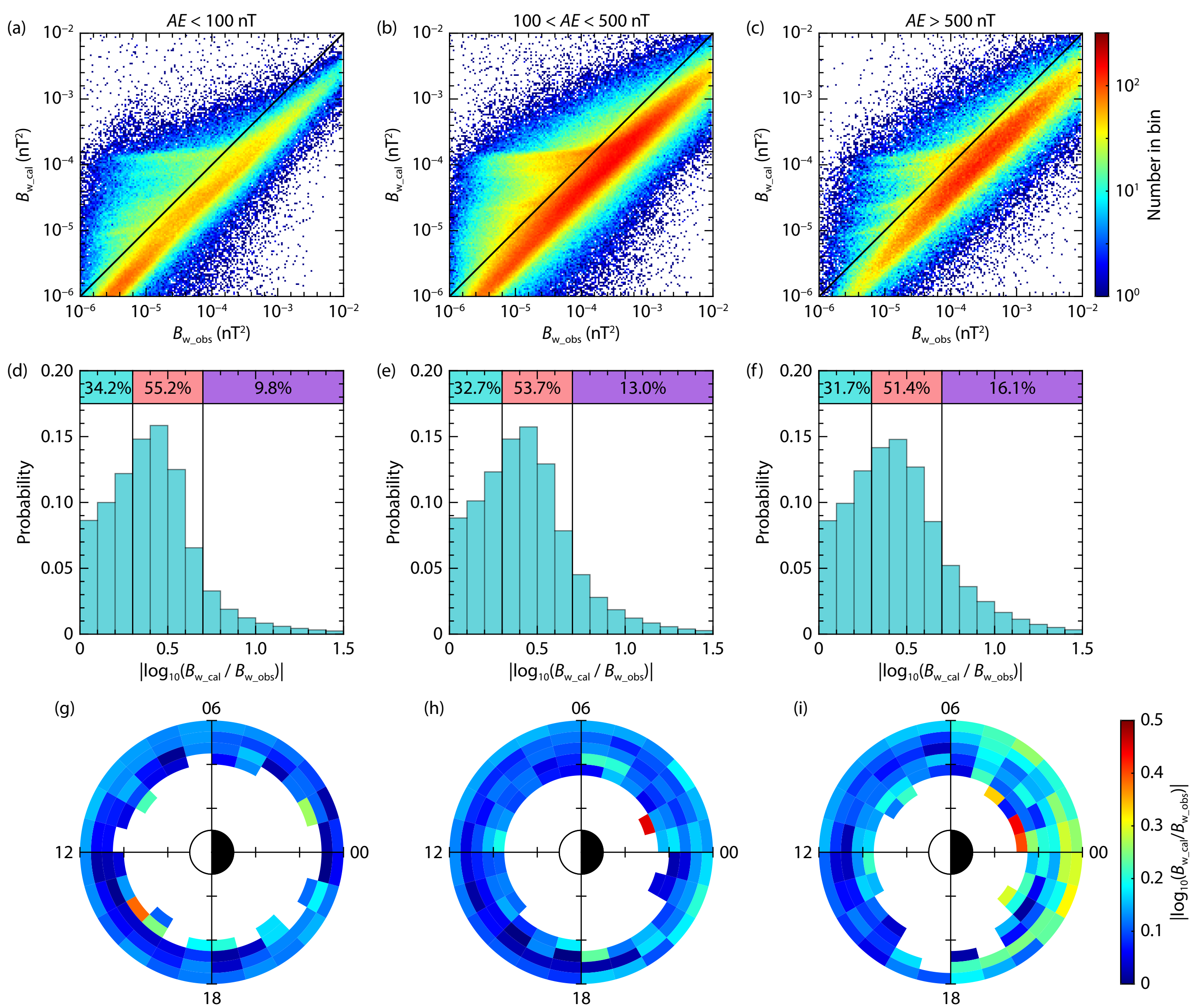

Figure 3. Same as Figure 2 but for different substorm activities.

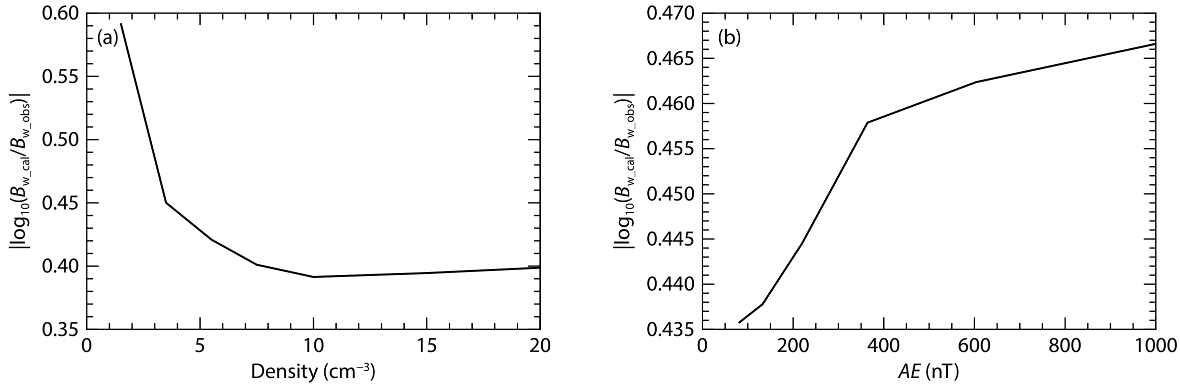

Figure 4. Distributions of $|\log_{10}(B_{\mathrm{w\_cal}}/B_{\mathrm{w\_obs}})|$ as a function of (a) the plasma density and (b) the geomagnetic activity.

netic activity increases, these regions expand substantially in both the radial and azimuthal directions. Therefore, these features again confirm that the validity of the cold plasma dispersion relation gradually decreases with the intensification of geomagnetic activity.

4. Electron Scattering Rates

The statistical results above clearly indicate that the cold plasma dispersion relation for chorus waves is less reliable over a wide region from the nightside to dayside through the dawnside, especially for low-density and active geomagnetic activity conditions. This unreliability probably strongly affects the chorus-driven electron scattering rates quantified by using the cold plasma dispersion relation. To investigate the applicability of the cold plasma dispersion relation in evaluating the electron scattering rates, we calculate electron scattering rates by using the statistical and theoretical dispersion relations of parallel propagating chorus waves and make a detailed comparison between them.

4.1 Plasma Density Effect on the Electron Scattering Rates

For representative, Figures 5a–5c present statistical plots of wave number versus frequency calculated by Equation (14) at $L = 5$ and magnetic latitude (MLAT) = 12° in three different plasma density ranges. The $L = 5$ is chosen because it is located within the heart of the radiation belt, whereas MLAT = 12° is chosen as a representative because calculating the bounce-averaged diffusion coefficients requires that the statistical dispersion curves be obtained and fitted at all latitudes where chorus waves occur. In each panel, the color shows the number of data points in each bin, the gray dashed line is the cold plasma dispersion curve, and the black solid and blue dashed lines are the averaged dispersion curve and its fitting value. The averaged dispersion curve does not coincide with the cold plasma theory, that is, the wave number obtained from the statistics is larger than that computed from the cold plasma hypothesis for a given wave frequency. In addition, the discrepancies between the averaged and the cold plasma dispersion curves decrease with an increase in plasma density. Thus, the scattering rates calculated by using the cold plasma dispersion relation will be inaccurate.

Figures 5d–5f show the bounce-averaged electron pitch angle scattering rates calculated by using the cold plasma dispersion relation in three different plasma density ranges. For comparison, Figures 5g–5i show the corresponding scattering rates calculated by using the fitted dispersion relation. Compared with the cold plasma dispersion relation, because the wave number obtained from the fitted dispersion relation is larger for a fixed wave frequency, the energy of resonant electrons is lower for the fitted dispersion relation in all three different plasma density ranges. Correspondingly, as shown in Figures 5g–5i, the resonant zone shifts toward lower energy and larger pitch angles. In addition to changing the resonant zone, the usage of the fitted dispersion relation substantially changes the scattering rates, and this change is highly energy and pitch angle dependent.

To quantify the deviations between the electron scattering rates calculated by using the two dispersion relations, we define a quantitative parameter:

$$\mathrm{Ratio} = \frac{\langle D_{\alpha\alpha\_\mathrm{cold}}\rangle - \langle D_{\alpha\alpha\_\mathrm{fit}}\rangle}{\langle D_{\alpha\alpha\_\mathrm{cold}}\rangle + \langle D_{\alpha\alpha\_\mathrm{fit}}\rangle}. \tag{15}$$

Therefore, a value close to 1 (−1) indicates that the scattering rates calculated by using the cold plasma dispersion relation are substantially large (ignorable small) compared with those calculated by using the fitted dispersion relation.

As shown in Figures 5j–5l, the scattering rates calculated by using the cold plasma dispersion relation are substantially larger at higher electron energies and at smaller pitch angles than those calculated by using the fitted dispersion relation. Furthermore, the usage of the cold plasma dispersion relation substantially underestimates the scattering rates at low electron energies and large pitch angles. Furthermore, a clear tendency can be seen that the area with pronounced discrepancies between these two scattering rates (|ratio| > 0.5) rapidly narrows as the plasma density increases. These discrepancies can be seen more clearly by the color-coded line plots shown in Figures 5m–5o for three given energies (i.e., 50, 100, and 500 keV). Compared with the usage of the fitted dispersion relation, the usage of the cold plasma dispersion relation overestimates the pitch angle scattering rates at small pitch angles and underestimates those at large pitch angles for all three given electron energies in all three different plasma density ranges. Overall, the discrepancies between these two scattering rates are less appreciable for all three given electron energies with the plasma density increasing, which can reach more than 2 orders of magnitude in the plasma density range of $N_e < 4$ cm^{-3} and rapidly drop down to several times in the plasma density

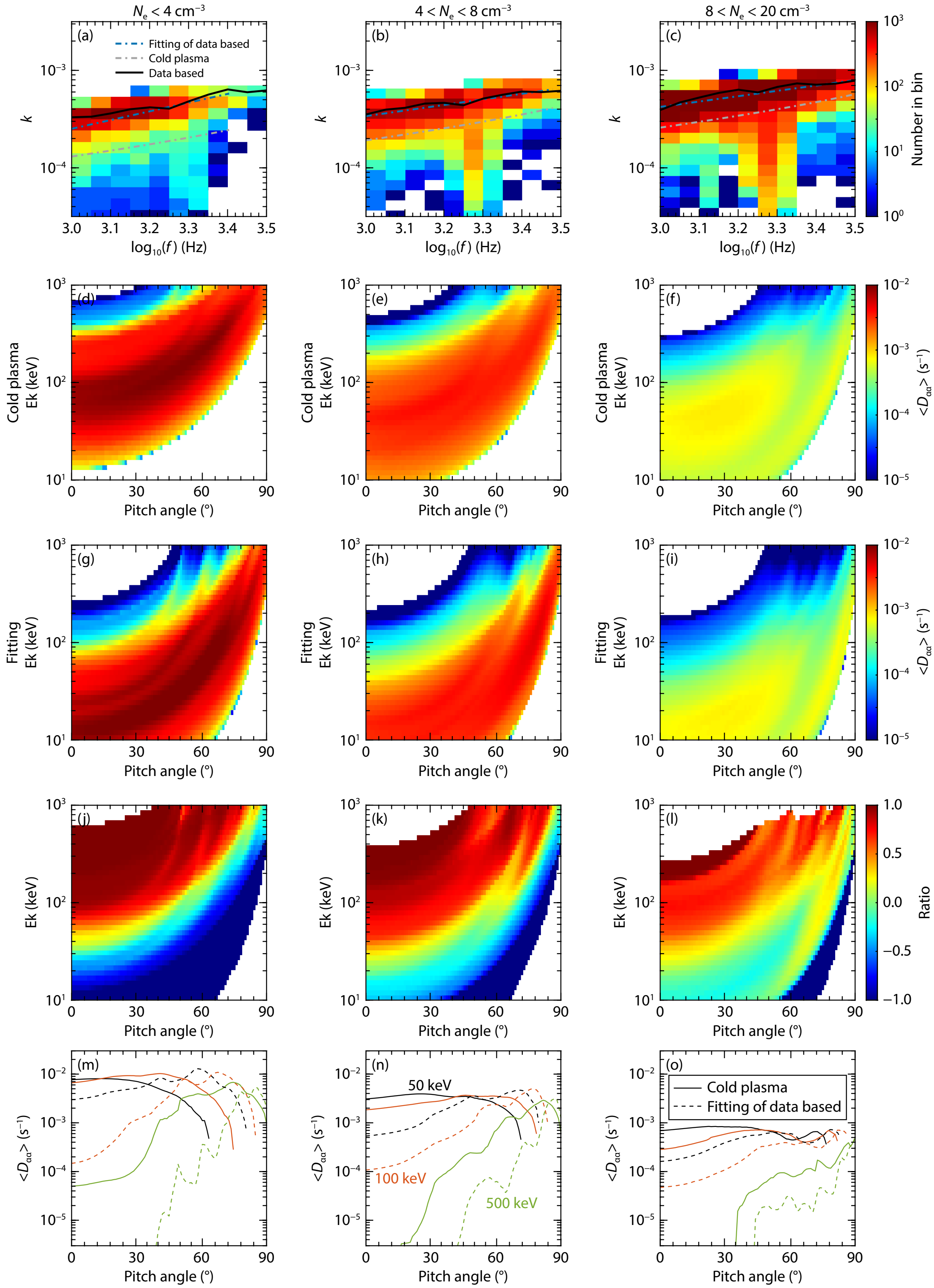

Figure 5. Comparison between the statistical and cold plasma dispersion relations together with the bounce-averaged electron pitch angle scattering rates calculated by them in three different plasma density ranges. (a–c) The statistical plot of wave number versus frequency calculated by Equation (14) at L = 5 and MLAT = 12°. The bounce-averaged electron pitch angle scattering rates calculated by using (d–f) the cold plasma dispersion relation and (g–i) the fitted dispersion relation as a function of pitch angle and electron energy. (j–l) The ratio in the same format as (d) to (i). (m–o) Line plots of bounce-averaged electron pitch angle scattering rates when using the cold plasma (solid lines) and fitted (dashed lines) dispersion relations for the three indicated electron energies. In (a) to (c), the color shows the number of data points in each bin, the gray dashed line is the cold plasma dispersion curve, and the black solid and blue dashed lines are, respectively, the averaged dispersion curve and its fitting value.

range $N_e > 8$ cm^{-3}.

4.2 Substorm Effect on the Electron Scattering Rates

Figure 6 shows the effect of substorm activities on the bounce-averaged electron scattering rates in the same format as Figure 5. As shown in Figures 6a–6c, the wave number obtained from the statistics is larger than that computed from the cold plasma hypothesis for a given wave frequency. The comparison between Figures 6d–6f and Figures 6j–6l shows large discrepancies in the bounce-averaged electron pitch angle scattering rates calculated by using the cold plasma dispersion relation and the fitted dispersion relation, consistent with the results of the ratio in Figures 6j–6l. Additionally, a clear tendency exists, namely, that the area with pronounced discrepancies between these two scattering rates (|ratio| > 0.5) rapidly expands as the geomagnetic activity increases. These discrepancies can be seen more clearly in the color-coded line plots shown in Figures 6m–6o for the three given energies (i.e., 50, 100, and 500 keV). Compared with the usage of the fitted dispersion relation, the usage of the cold plasma dispersion relation overestimates the pitch angle scattering rates at small pitch angles and underestimates those rates at large pitch angles for all three given electron energies in all three different geomagnetic activity conditions.

5. Conclusions and Discussion

In this study, by using the Van Allen Probe observations from 2012 to 2018, we investigate the validity of the cold plasma dispersion relation for different plasma density ranges and geomagnetic activity levels. By fitting the data-based dispersion relation, the electron bounce-averaged pitch angle scattering rates are calculated, which are compared with those calculated by using the cold plasma approximation. The main conclusions can be summarized as follows:

(1) Overall, the observed magnetic field intensities of the chorus waves are larger than those calculated from the cold plasma dispersion relation. The comparison between these two intensities shows that the validity of the cold plasma dispersion relation decreases with a decrease in plasma density or an enhancement of geomagnetic activity.

(2) The regions where the cold plasma dispersion relation is unreliable are mainly concentrated in the nightside, and they expand in both the radial and azimuthal directions as the geomagnetic activity intensifies or the background plasma density decreases.

(3) Substantial differences are found in the electron bounce-averaged pitch angle scattering rates calculated by the fitted and cold plasma dispersion relations. Specifically, the usage of the cold plasma dispersion relation not only overestimates the minimum resonant energy but also significantly underestimates (overestimates) the scattering rates at low (high) electron energies and large (small) pitch angles. These differences become more pronounced as the electron density decreases or the geomagnetic activity intensifies.

The presence of warm or hot electrons may cause the deviation of the real dispersion relation from the cold plasma dispersion relation for the chorus wave. Theoretically, the cold plasma dispersion relation is less reliable if the warm or hot electrons are richer (Chen LJ et al., 2013). Generally, the proportion of warm or hot electrons is greater in regions with lower electron densities and results in lesser validity of the cold plasma dispersion relation. In addition, many more warm or hot electrons are injected into the chorus source regions from the plasma sheet as the substorm activity intensifies. Thus, the percentage of warm or hot electrons is greatly enhanced, which accounts for the serious breakdown of the cold plasma dispersion relation during periods of geomagnetic disturbance. The warm or hot electrons are injected from the nightside and drift toward noonside through the dawnside, resulting in an increase in their proportion in these regions. Consequently, the cold plasma dispersion relation is more unreliable in these regions, consistent with the statistical results in Figures 2g–2i and Figures 3g–3i. In addition to the warm or hot electrons, the cold plasma approximation of the background electron plasma, namely, whether the electrons can be assumed to be cold, may be another potential contributor to the deviation. However, the deviation coming from this approximation is not important here because such a deviation is mainly located at high-frequency regions (e.g., >0.8 f_{ce} at $L = 5$ for $N_e = 10$ cm^{-3}), which is beyond the frequency range of our study (not shown here).

In this study, a detailed analysis of the validity of the cold plasma dispersion relation for chorus waves is carried out based on the observed data. Nevertheless, it should be noted that the plasma density inferred from the upper hybrid resonance frequency is inaccurate because of the accuracy limitation of the instrumental measurement and the inaccurate identification of the upper hybrid resonance frequency. In addition, wave detection can be affected by the sheath impedance effects between the sensor and the surrounding plasma. These two factors will affect the test of the validity of the cold plasma dispersion relation and should be taken into account in the future.

It should be noted that large deviations occur at a low L-shell in the dawnside regions when the plasma density lowers to more than 4 cm^{-3}, as shown in Figure 2g. It is probably caused for the following reason. Generally, the plasma density decreases exponentially with an increasing L-shell. However, the statistical results show that the plasma densities at low L-shells are very low, even comparable to those at high L-shells. This indicates that the plasmasphere is substantially eroded and that the geomagnetic activity is probably at a higher level during the measurements at lower L-shells. Stronger geomagnetic activity raises the proportion of warm or hot particles, resulting in more substantial deviations from the cold plasma approximation in the low L-shell regions.

Acknowledgments

The Van Allen Probe data are available at https://emfisis.physics.uiowa.edu/data/index for the EMFISIS. Solar wind parameters and geomagnetic indices are available at https://cdaweb.sci.gsfc.nasa.gov/index.html/. This work is supported by the National Natural Science Foundation of China (NSFC) through Grant Number 42074193.

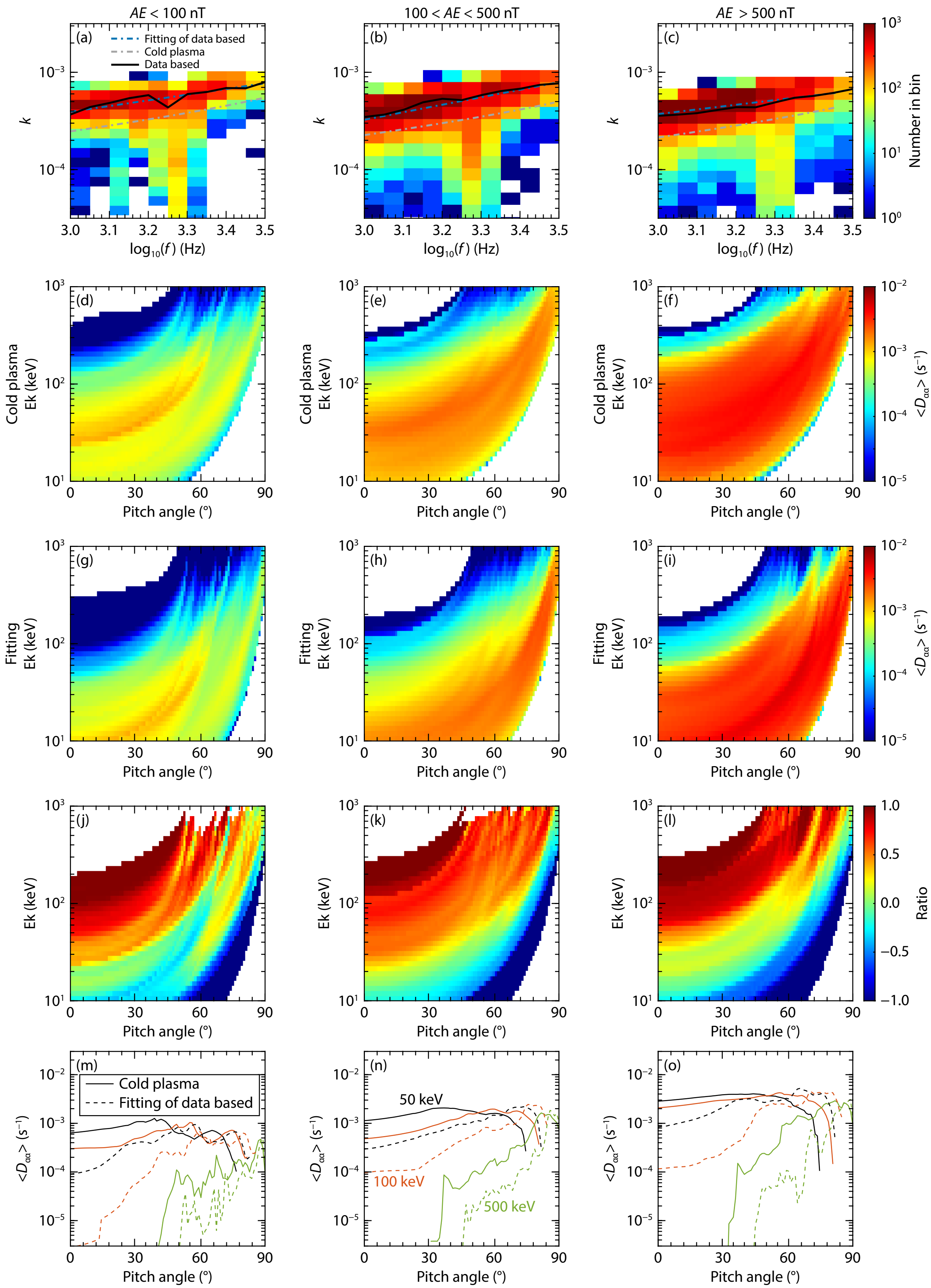

Figure 6. Same as Figure 5 but for different substorm activities.

References

Albert, J. M. (2005). Evaluation of quasi-linear diffusion coefficients for whistler mode waves in a plasma with arbitrary density ratio. *J. Geophys. Res.: Space Phys.*, *110*(A3), A03218. https://doi.org/10.1029/2004JA010844

Anderson, R. R., and Maeda, K. (1977). VLF emissions associated with enhanced magnetospheric electrons. *J. Geophys. Res.*, *82*(1), 135–146. https://doi.org/10.1029/ja082i001p00135

Bortnik, J., and Thorne, R. M. (2007). The dual role of ELF/VLF chorus waves in the acceleration and precipitation of radiation belt electrons. *J. Atmos. Sol. Terr. Phys.*, *69*(3), 378–386. https://doi.org/10.1016/j.jastp.2006.05.030

Cao, J. B., Liu, Z. X., Yang, J. Y., Yian, C. X., Wang, Z. G., Zhang, X. H., Wang, S. R., Chen, S. W., Bian, W., … Mazelle, C. (2005). First results of low frequency electromagnetic wave detector of TC-2/Double Star program. *Ann. Geophys.*, *23*(8), 2803–2811. https://doi.org/10.5194/angeo-23-2803-2005

Cao, J. B., Yang, J. Y., Yan, C. X., and Li, L. Y. (2007). The observations of high energy electrons and associated waves by DSP satellites during substorm. *Nucl. Phys. B: Proc. Suppl.*, *166*, 56–61. https://doi.org/10.1016/j.nuclphysbps.2006.12.066

Cao, X., Ni, B. B., Summers, D., Fu, S., Gu, X. D., and Shi, R. (2020). Hot plasma effects on the pitch-angle scattering rates of radiation belt electrons due to plasmaspheric hiss. *Astrophys. J.*, *896*(2), 118. https://doi.org/10.3847/1538-4357/ab9107

Chen, H. Y., Gao, X. L., Lu, Q. M., Sauer, K., Chen, R., Yao, J. S., and Wang, S. (2021). Gap formation around 0.5Ω_e of whistler-mode waves excited by electron temperature anisotropy. *J. Geophys. Res.: Space Phys.*, *126*(2), e2020JA028631. https://doi.org/10.1029/2020JA028631

Chen, L. J., Thorne, R. M., Shprits, Y., and Ni, B. B. (2013). An improved dispersion relation for parallel propagating electromagnetic waves in warm plasmas: Application to electron scattering. *J. Geophys. Res.: Space Phys.*, *118*(5), 2185–2195. https://doi.org/10.1002/jgra.50260

Chen, L. J., Zhu, H., and Zhang, X. J. (2019). Wavenumber analysis of EMIC waves. *Geophys. Res. Lett.*, *46*(11), 5689–5697. https://doi.org/10.1029/2019GL082686

Chen, Z. Z., Yu, J., Wang, J., He, Z. G., Liu, N. G., Cui, J., and Cao, J. B. (2022). High-frequency electrostatic waves modulated by whistler waves behind dipolarization front. *J. Geophys. Res.: Space Phys.*, *127*(11), e2022JA030935. https://doi.org/10.1029/2022JA030935

Fu, H. S., Cao, J. B., Mozer, F. S., Lu, H. Y., and Yang, B. (2012). Chorus intensification in response to interplanetary shock. *J. Geophys. Res.: Space Phys.*, *117*(A1), A01203. https://doi.org/10.1029/2011JA016913

Fu, X. R., Guo, Z. H., Dong, C. F., and Gary, S. P. (2015). Nonlinear subcyclotron resonance as a formation mechanism for gaps in banded chorus. *Geophys. Res. Lett.*, *42*(9), 3150–3159. https://doi.org/10.1002/2015GL064182

Gao, X. L, Li, W., Thorne, R. M., Bortnik, J., Angelopoulos, V., Lu, Q. M., Tao, X., and Wang, S. (2014). New evidence for generation mechanisms of discrete and hiss-like whistler mode waves. *Geophys. Res. Lett.*, *41*(14), 4805–4811. https://doi.org/10.1002/2014GL060707

Gao, X. L., Li, W., Bortnik, J., Thorne, R. M., Lu, Q. M., Ma, Q. L., Tao, X., and Wang, S. (2015). The effect of different solar wind parameters upon significant relativistic electron flux dropouts in the magnetosphere. *J. Geophys. Res.: Space Phys.*, *120*(6), 4324–4337. https://doi.org/10.1002/2015JA021182

Gao, X. L., Lu, Q. M., Bortnik, J., Li, W., Chen, L. J., and Wang, S. (2016). Generation of multiband chorus by lower band cascade in the Earth's magnetosphere. *Geophys. Res. Lett.*, *43*(6), 2343–2350. https://doi.org/10.1002/2016GL068313

Gao, X. L., Chen, R., Lu, Q. M., Chen, L. J., Chen, H. Y., and Wang, X. Y. (2022). Observational evidence for the origin of repetitive chorus emissions. *Geophys. Res. Lett.*, *49*(12), e2022GL099000. https://doi.org/10.1029/2022GL099000

Gao, X. L., Ma, J. Q., Shao, T., Chen, R., Ke, Y. G., and Lu, Q. M. (2024). Why chorus waves are the dominant driver for diffuse auroral precipitation. *Sci. Bull.*, *69*(5), 597–600. https://doi.org/10.1016/j.scib.2023.12.009

Glauert, S. A., and Horne, R. B. (2005). Calculation of pitch angle and energy diffusion coefficients with the PADIE code. *J. Geophys. Res.: Space Phys.*, *110*(A4), A04206. https://doi.org/10.1029/2004JA010851

Hartley, D. P., Chen, Y., Kletzing, C. A., Denton, M. H., and Kurth, W. S. (2015). Applying the cold plasma dispersion relation to whistler mode chorus waves: EMFISIS wave measurements from the Van Allen Probes. *J. Geophys. Res.: Space Phys.*, *120*(2), 1144–1152. https://doi.org/10.1002/2014JA020808

Hartley, D. P., Kletzing, C. A., Kurth, W. S., Bounds, S. R., Averkamp, T. F., Hospodarsky, G. B., Wygant, J. R., Bonnell, J. W., Santolík, O., and Watt, C. E. J. (2016). Using the cold plasma dispersion relation and whistler mode waves to quantify the antenna sheath impedance of the Van Allen Probes EFW instrument. *J. Geophys. Res.: Space Phys.*, *121*(5), 4590–4606. https://doi.org/10.1002/2016JA022501

He, Z. G., Yan, Q., Chu, Y. C., and Cao, Y. (2016). Wave-driven gradual loss of energetic electrons in the slot region. *J. Geophys. Res.: Space Phys.*, *121*(9), 8614–8623. https://doi.org/10.1002/2016JA023087

Horne, R. B., Thorne, R. M., Shprits, Y. Y., Meredith, N. P., Glauert, S. A., Smith, A. J., Kanekal, S. G., Baker, D. N., Engebretson, M. J., … Decreau, P. M. E. (2005). Wave acceleration of electrons in the Van Allen radiation belts. *Nature*, *437*(7056), 227–230. https://doi.org/10.1038/nature03939

Kennel, C. F., and Engelmann, F. (1966). Velocity space diffusion from weak plasma turbulence in a magnetic field. *Phys. Fluids*, *9*(12), 2377–2388. https://doi.org/10.1063/1.1761629

Kletzing, C. A., Kurth, W. S., Acuna, M., MacDowall, R. J., Torbert, R. B., Averkamp, T., Bodet, D., Bounds, S. R., Chutter, M., … Tyler, J. (2013). The Electric and Magnetic Field Instrument Suite and Integrated Science (EMFISIS) on RBSP. *Space Sci. Rev.*, *179*(1-4), 127–181. https://doi.org/10.1007/s11214-013-9993-6

Kurth, W. S., de Pascuale, S., Faden, J. B., Kletzing, C. A., Hospodarsky, G. B., Thaller, S., and Wygant, J. R. (2015). Electron densities inferred from plasma wave spectra obtained by the Waves instrument on Van Allen Probes. *J. Geophys. Res.: Space Phys.*, *120*(2), 904–914. https://doi.org/10.1002/2014JA020857

Li, L. Y., Yu, J., Cao, J. B., Zhang, D., Wei, X. H., Rong, Z. J., Yang, J. Y., and Fu, H. S. (2013). Rapid loss of the plasma sheet energetic electrons associated with the growth of whistler mode waves inside the bursty bulk flows. *J. Geophys. Res.: Space Phys.*, *118*(11), 7200–7210. https://doi.org/10.1002/2013JA019109

Li, L. Y., Yu, J., Cao, J. B., Yang, J. Y., Li, X., Baker, D. N., Reeves, G. D., and Spence, H. (2017). Roles of whistler mode waves and magnetosonic waves in changing the outer radiation belt and the slot region. *J. Geophys. Res.: Space Phys.*, *122*(5), 5431–5448. https://doi.org/10.1002/2016JA023634

Li, L. Y., Yu, J., Cao, J. B., Chen, L. J., Reeves, G. D., and Blake, J. B. (2022). Competitive influences of different plasma waves on the pitch angle distribution of energetic electrons inside and outside plasmasphere. *Geophys. Res. Lett.*, *49*(1), e2021GL096062. https://doi.org/10.1029/2021GL096062

Li, W., Thorne, R. M., Meredith, N. P., Horne, R. B., Bortnik, J., Shprits, Y. Y., and Ni, B. (2008). Evaluation of whistler mode chorus amplification during an injection event observed on CRRES. *J. Geophys. Res.: Space Phys.*, *113*(A9), A09210. https://doi.org/10.1029/2008JA013129

Li, W., Thorne, R. M., Angelopoulos, V., Bonnell, J. W., McFadden, J. P., Carlson, C. W., Lecontel, O., Roux, A., Glassmeier, K. H., and Auster, H. U. (2009). Evaluation of whistler-mode chorus intensification on the nightside during an injection event observed on the THEMIS spacecraft. *J. Geophys. Res.: Space Phys.*, *114*(A1), A00C14. https://doi.org/10.1029/2008JA013554

Liu, X., and Chen, L. J. (2019). Instability in a relativistic magnetized plasma. *Phys. Plasmas*, *26*(4), 042902. https://doi.org/10.1063/1.5089749

Liu, X., Gu, W. Y., Xia, Z. Y., Chen, L. J., and Horne, R. B. (2021). Frequency-dependent modulation of whistler-mode waves by density irregularities during the recovery phase of a geomagnetic storm. *Geophys. Res. Lett.*, *48*(16), e2021GL093095. https://doi.org/10.1029/2021GL093095

Lu, Q. M., Ke, Y. G., Wang, X. Y., Liu, K. J., Gao, X. L., Chen, L. J., and Wang, S. (2019). Two-dimensional gcPIC simulation of rising-tone chorus waves in a dipole magnetic field. *J. Geophys. Res.: Space Phys.*, *124*(6), 4157–4167. https://doi.org/10.1029/2019JA026586

Lu, Q. M., Chen, L. J., Wang, X. Y., Gao, X. L., Lin, Y., and Wang, S. (2021). Repetitive emissions of rising-tone chorus waves in the inner magnetosphere. *Geophys. Res. Lett.*, *48*(15), e2021GL094979. https://doi.org

/10.1029/2021GL094979

Ma, X., Cao, X., Ni, B. B., Zhu, Q., and Xiang, Z. (2021). Realistic dispersion of plasmaspheric hiss in the inner magnetosphere and its effect on wave-induced electron scattering rates. *Astrophys. J.*, *916*(1), 14. https://doi.org/10.3847/1538-4357/abf4d6

Meredith, N. P., Horne, R. B., and Anderson, R. R. (2001). Substorm dependence of chorus amplitudes: Implications for the acceleration of electrons to relativistic energies. *J. Geophys. Res.: Space Phys.*, *106*(A7), 13165–13178. https://doi.org/10.1029/2000ja900156

Meredith, N. P., Horne, R. B., Thorne, R. M., and Anderson, R. R. (2003). Favored regions for chorus-driven electron acceleration to relativistic energies in the Earth's outer radiation belt. *Geophys. Res. Lett.*, *30*(16), 1871. https://doi.org/10.1029/2003GL017698

Meredith, N. P., Horne, R. B., Sicard-Piet, A., Boscher, D., Yearby, K. H., Li, W., and Thorne, R. M. (2012). Global model of lower band and upper band chorus from multiple satellite observations. *J. Geophys. Res.: Space Phys.*, *117*(A10), A10225. https://doi.org/10.1029/2012JA017978

Ni, B. B., Thorne, R. M., Shprits, Y. Y., and Bortnik, J. (2008). Resonant scattering of plasma sheet electrons by whistler-mode chorus: Contribution to diffuse auroral precipitation. *Geophys. Res. Lett.*, *35*(11), L11106. https://doi.org/10.1029/2008GL034032

Ni, B. B., Thorne, R. M., Meredith, N. P., Horne, R. B., and Shprits, Y. Y. (2011). Resonant scattering of plasma sheet electrons leading to diffuse auroral precipitation: 2. Evaluation for whistler mode chorus waves. *J. Geophys. Res.: Space Phys.*, *116*(A4), A04219. https://doi.org/10.1029/2010JA016233

Ni, B. B., Hua, M., Zhou, R. X., Yi, J., and Fu, S. (2017). Competition between outer zone electron scattering by plasmaspheric hiss and magnetosonic waves. *Geophys. Res. Lett.*, *44*(8), 3465–3474. https://doi.org/10.1002/2017GL072989

Omura, Y., Hikishima, M., Katoh, Y., Summers, D., and Yagitani, S. (2009). Nonlinear mechanisms of lower-band and upper-band VLF chorus emissions in the magnetosphere. *J. Geophys. Res.: Space Phys.*, *114*(A7), A07217. https://doi.org/10.1029/2009JA014206

Roth, I., Temerin, M., and Hudson, M. K. (1999). Resonant enhancement of relativistic electron fluxes during geomagnetically active periods. *Ann. Geophys.*, *17*(5), 631–638. https://doi.org/10.1007/s00585-999-0631-2

Santolík, O., Gurnett, D. A., Pickett, J. S., Parrot, M., and Cornilleau-Wehrlin, N. (2003a). Spatio-temporal structure of storm-time chorus. *J. Geophys. Res.: Space Phys.*, *108*(A7), 1278. https://doi.org/10.1029/2002JA009791

Santolík, O., Parrot, M., and Lefeuvre, F. (2003b). Singular value decomposition methods for wave propagation analysis. *Radio Sci.*, *38*(1), 1010. https://doi.org/10.1029/2000RS002523

Sheeley, B. W., Moldwin, M. B., Rassoul, H. K., and Anderson, R. R. (2001). An empirical plasmasphere and trough density model: CRRES observations. *J. Geophys. Res.: Space Phys.*, *106*(A11), 25631–25641. https://doi.org/10.1029/2000ja000286

Shprits, Y., Daae, M., and Ni, B. B. (2012). Statistical analysis of phase space density buildups and dropouts. *J. Geophys. Res.: Space Phys., 117*(A1), A01219. https://doi.org/10.1029/2011JA016939

Su, Z. P., Zheng, H. N., and Wang, S. (2009). Evolution of electron pitch angle distribution due to interactions with whistler mode chorus following substorm injections. *J. Geophys. Res.: Space Phys.*, *114*(A8), A08202. https://doi.org/10.1029/2009JA014269

Su, Z. P., Zheng, H. N., and Wang, S. (2010). A parametric study on the diffuse auroral precipitation by resonant interaction with whistler mode chorus. *J. Geophys. Res.: Space Phys.*, *115*(A5), A05219. https://doi.org/10.1029/2009JA014759

Summers, D., and Ma, C. Y. (2000). A model for generating relativistic electrons in the Earth's inner magnetosphere based on gyroresonant wave-particle interactions. *J. Geophys. Res.: Space Phys.*, *105*(A2), 2625–2639. https://doi.org/10.1029/1999ja900444

Summers, D. (2005). Quasi-linear diffusion coefficients for field-aligned electromagnetic waves with applications to the magnetosphere. *J. Geophys. Res.: Space Phys.*, *110*(A8), A08213. https://doi.org/10.1029/2005JA011159

Thorne, R. M. (2010). Radiation belt dynamics: The importance of wave-particle interactions. *Geophys. Res. Lett.*, *37*(22), L22107. https://doi.org/10.1029/2010GL044990

Thorne, R. M., Li, W., Ni, B., Ma, Q., Bortnik, J., Chen, L., Baker, D. N., Spence, H. E., Reeves, G. D., … Kanekal, S. G. (2013). Rapid local acceleration of relativistic radiation-belt electrons by magnetospheric chorus. *Nature*, *504*(7480), 411–414. https://doi.org/10.1038/nature12889

Tsurutani, B. T., and Smith, E. J. (1974). Postmidnight chorus: A substorm phenomenon. *J. Geophys. Res.*, *79*(1), 118–127. https://doi.org/10.1029/ja079i001p00118

Tsurutani, B. T., and Smith, E. J. (1977). Two types of magnetospheric ELF chorus and their substorm dependences. *J. Geophys. Res.*, *82*(32), 5112–5128. https://doi.org/10.1029/ja082i032p05112

Wang, J., Yu, J., Chen, Z. Z., Xu, X. J., Li, K., Cui, J., and Cao, J. B. (2023a). MAVEN observations of whistler-mode waves within the magnetic dips in the Martian ionopause/ionosphere. *Astron. J.*, *165*(2), 56. https://doi.org/10.3847/1538-3881/aca802

Wang, J., Yu, J., Ren, A. J., Chen, Z. Z., Xu, X. J., Cui, J., and Cao, J. B. (2023b). In situ observations of whistler-mode waves in magnetic reconnection at Mars. *Astrophys. J.*, *944*(1), 85. https://doi.org/10.3847/1538-4357/acb152

Xiao, F. L., Yang, C., He, Z. G., Su, Z. P., Zhou, Q. H., He, Y. H., Kletzing, C. A., Kurth, W. S., Hospodarsky, G. B., … Wygant, J. R. (2014). Chorus acceleration of radiation belt relativistic electrons during March 2013 geomagnetic storm. *J. Geophys. Res.: Space Phys.*, *119*(5), 3325–3332. https://doi.org/10.1002/2014JA019822

Yu, J., Li, L. Y., Cao, J. B., Chen, L., Wang, J., and Yang, J. (2017). Propagation characteristics of plasmaspheric hiss: Van Allen Probe observations and global empirical models. *J. Geophys. Res.: Space Phys.*, *122*(4), 4156–4167. https://doi.org/10.1002/2016JA023372

Yu, J., Li, L. Y., Cui, J., and Wang, J. (2018). Ultrawideband rising-tone chorus waves observed inside the oscillating plasmapause. *J. Geophys. Res.: Space Phys.*, *123*(8), 6670–6678. https://doi.org/10.1029/2018JA025875

Yu, J., Li, L. Y., Cui, J., Cao, J. B., and Wang, J. (2019a). Combined effects of equatorial chorus waves and high-latitude Z-mode waves on Saturn's radiation belt electrons. *Geophys. Res. Lett.*, *46*(15), 8624–8632. https://doi.org/10.1029/2019GL084004

Yu, J., Li, L. Y., Cui, J., Cao, J. B., and Wang, J. (2019b). Effect of hot He^+ ions on the electron pitch angle scattering driven by H^+, He^+, and O^+ band EMIC waves. *Geophys. Res. Lett.*, *46*(12), 6306–6314. https://doi.org/10.1029/2019GL083456

Yu, J., Wang, J., Li, L. Y., Cui, J., Cao, J. B., and He, Z. G. (2020a). Electron diffusion by coexisting plasmaspheric hiss and chorus waves: Multisatellite observations and simulations. *Geophys. Res. Lett.*, *47*(15), e2020GL088753. https://doi.org/10.1029/2020GL088753

Yu, J., Li, L. Y., Cui, J., Cao, J. B., Wang, J., He, Z. G., and Yang, J. (2020b). Nonlinear interactions between relativistic electrons and EMIC waves in magnetospheric warm plasma environments. *J. Geophys. Res.: Space Phys.*, *125*(12), e2020JA028089. https://doi.org/10.1029/2020JA028089

Yu, J., Wang, J., He, Z. G., Liu, N. G., Li, K., Ren, A. J., Li, L. Y., Cui, J., and Cao, J. B. (2022). Combined scattering of suprathermal electrons by whistler-mode chorus and electromagnetic ion cyclotron waves in the low-density plasmatrough. *J. Geophys. Res.: Space Phys.*, *127*(8), e2022JA030640. https://doi.org/10.1029/2022JA030640

Yu, J., Ren, A. J., He, Z. G., Liu, X. M., Wang, J., Liu, N. G., Chen, Z. Z., Li, L. Y., Cui, J., and Cao, J. B. (2024). Resonant interactions between relativistic electrons and EMIC waves modified by partial shell proton velocity distributions. *J. Geophys. Res.: Space Phys.*, *129*(4), e2023JA032355. https://doi.org/10.1029/2023JA032355

Zhima, Z., Cao, J. B., Liu, W. L., Fu, H. S., Wang, T. Y., Zhang, X. M., and Shen, X. H. (2014). Storm time evolution of ELF/VLF waves observed by DEMETER satellite. *J. Geophys. Res.: Space Phys.*, *119*(4), 2612–2622. https://doi.org/10.1002/2013JA019237